Materials Characterization 131 (2017) 21–30

Contents lists available at ScienceDirect

Materials Characterization

journal homepage: www.elsevier.com/locate/matchar

Precipitation in simultaneously nitrided and aged Mo-containing maraging steel

An Verdiere[a,*], Christina Hofer[b], Sam De Waele[a,c], Vitaliy Bliznuk[a], Sophie Primig[b,d], Stefaan Cottenier[a,c], Minh Duc Tran[e], Bert Pennings[e], Leo A.I. Kestens[a,f], Roumen H. Petrov[a,f]

[a] Department of Materials Science and Engineering, UGent, Belgium
[b] Department of Physical Metallurgy and Materials Testing, Montanuniversität Leoben, Austria
[c] Center for Molecular Modeling, UGent, Belgium
[d] School of Materials Science and Engineering, University of New South Wales, Australia
[e] Bosch Transmission Technology, Advanced Engineering, Tilburg, The Netherlands
[f] Department of Materials Science and Engineering, TUDelft, The Netherlands

ARTICLE INFO

Keywords:
Nitriding
Maraging steel
Precipitation
Transmission electron microscopy (TEM)
Atom probe tomography (APT)
Density functional theory (DFT)

ABSTRACT

The excellent mechanical properties of maraging steels are ascribed to nanometer-sized intermetallics which precipitate during aging in the ductile very low carbon Ni-martensite. Their wear and fatigue properties can be improved by nitriding. The non-equilibrium precipitation reactions in Fe-Ni-Co-Mo maraging steels are studied during an aging heat treatment executed in a nitriding atmosphere. The precipitates formed during the initial stages of precipitation are characterized with transmission electron microscopy and atom probe tomography. Spherical intermetallic precipitates having a diameter of around 3 nm were detected in the aged, bulk material. These ω-type precipitates formed during the early stages of aging, have a trigonal crystal lattice and their chemical composition is close to $(Fe,Ni)_7Mo_2$. In the nitrided layer, Mo-N disc-shaped nitrides on the {100} martensitic lattice having a diameter of 3 to 4 nm were found but their exact crystal structure could not be determined with microstructural characterization techniques. Density functional theory calculations confirmed that a single layer of Mo atoms, substituting Fe on the {100} plane of the Fe-matrix, is stable and showed that the N atoms prefer to be in the Mo-layer, on the octahedral sites with Fe as nearest neighbors.

1. Introduction

One of the best combinations of high strength and toughness in engineering alloys can be found in maraging steels. These very low carbon Fe-Ni alloys are strengthened by homogeneously distributed nanometer-sized intermetallics which are formed during the final aging step [1]. After quenching, soft and ductile lath martensite containing a high density of dislocations is formed. Nucleation of intermetallic precipitates during the aging step can occur quickly on these dislocations and the growth can proceed by dislocations serving as diffusion channels for solute atoms from the matrix [2]. However, randomly distributed precipitates throughout the matrix were also reported in maraging steels aged below 450 °C [3]. For several high performance applications such as aerospace and tooling, Fe-Ni-Co-Mo maraging steels are used due to their excellent mechanical properties and especially fatigue response even in the very high cycle fatigue domain [4].

A number of studies on aging in Fe-Ni-Co-Mo maraging steels have been carried out [3,5,6], but the current knowledge concerning the precursor phases formed during the early stages of precipitation is not yet complete. Main difficulties in the characterization are the ultrafine scale of the microstructure, absence of stable equilibrium phases and closely matching crystal structures and interplanar spacings of the phases [6]. Observed intermetallics in these Ti-free maraging steels are initially the metastable and coherent ω-phase, followed by Ni_3Mo at the earlier aging stage [1,7], and more stable Fe_7Mo_6 after prolonged aging [8].

Due to the absence of carbides, one of the limitations of maraging steels is the moderate wear resistance in comparison to conventional tool steels [9]. To improve their performance in severe loading conditions, the case can be additionally hardened e.g. by nitriding. During this low temperature thermochemical treatment, atomic N diffuses into the material, resulting in an increased surface hardness, wear and fatigue resistance. In general, a compound layer consisting of ε and/or γ' Fe-nitrides and an underlying nitrogen diffusion zone are formed during nitriding. The compound layer improves tribological and anticorrosion properties but it can be undesirable due to its porosity and brittleness.

* Corresponding author.
E-mail address: an.verdiere@ugent.be (A. Verdiere).

http://dx.doi.org/10.1016/j.matchar.2017.06.014
Received 29 October 2016; Received in revised form 12 June 2017; Accepted 12 June 2017
Available online 13 June 2017
1044-5803/

Therefore, in many industrial applications the formation of this compound layer is minimized or avoided by controlling the process parameters, especially the nitriding potential in the case of gas nitriding [10,11].

Steels containing alloying elements with a high affinity for nitrogen form finely dispersed and hard alloying element nitrides in the diffusion zone. These nitrides effectively contribute to the strengthening, while diffused nitrogen in the supersaturated diffusion zone is only responsible for a very small solid-solution strengthening effect [12]. Due to the volumetric misfit between the matrix and these fine nitrides, strain fields surrounding the precipitates develop. In order to counteract the desired expansion, compressive residual stresses evolve and contribute significantly to improving the fatigue resistance [13]. The alloying elements are classified by the Me-N interaction parameter, defined as the ratio (per unit volume of precipitate) of the Gibbs energy of formation of the precipitate and the misfit-strain energy induced in the precipitate/matrix system [10]. Alloying elements such as Ti, V and Cr having a strong Me-N interaction can instantaneously precipitate [14], while alloying elements such as Al, Si and Mo have a weaker interaction because of a large volume misfit. The latter will only precipitate when the N supersaturation in the surface layer is high enough [12] and the precipitation proceeds through a sequence of metastable phases until the equilibrium phase is reached [15]. Besides, the precipitation can be enhanced by the presence of dislocations in the matrix [10].

Several studies on nitriding of Mo-containing steels have been conducted and many different compositions of intermediate and equilibrium nitrides were identified. It is reported that during nitriding, the morphology of the precipitates changes from thin coherent platelets through semi-coherent plates to incoherent spheres [16]. The sequence of precipitation is proposed in [15] as changing respectively from bct $(Fe,Mo)_{16}N_2$ [17], to fcc $(Fe,Mo)_6N_2$ and finally fcc $(Mo,Fe)_2N$ or (Mo,Fe)N. Different compositions for the metastable interstitial-substitutional solute-atom clusters $Fe_xMo_yN_z$ can be found [18]. However, some authors suggest that the presence of Fe in the nitrides might be due to the limited spatial resolution of the field ion microscopy-atom probe analyses, on which most of the composition data are based [19–21]. The interaction of nitride precipitation and precipitation of intermetallic compounds in the depth direction, e.g. [22] will not be discussed in this paper.

Although the nitriding process is very well studied, there is little research on the precipitation behavior of Mo-nitrides in Mo-containing maraging steels, especially for short nitriding times. This is also the case for the formation of the precursor phases during aging in these steels. Information about the degree of coherency and the composition of the precipitates helps to understand the microstructure-property relationships in nitrided maraging steels. In this study, the precipitates formed during an aging heat treatment executed in a nitriding atmosphere during the initial stages of precipitation, are characterized with transmission electron microscopy (TEM) and atom probe tomography (APT). Density functional theory (DFT) calculations are used to confirm and specify the atomic structure of the nitrides.

2. Experimental Setup and Calculation Details

The studied maraging steel has the following nominal composition (wt%): 18 Ni, 16.5 Co, 5 Mo and balance Fe. Thin strips of this steel were 50% cold rolled from the as-delivered sheet and air-quenched after annealing at 840 °C in a protective atmosphere. This heat treatment generates a fully martensitic structure without retained austenite. In order to determine the peak-hardness, aging heat treatments were performed in a salt bath for various aging times at a temperature of 470 ± 5 °C. Vickers hardness was measured on a Zwick hardness tester with a load of 200 g (HV 0.2). Based on these results, the nitriding conditions were selected. After cleaning and degreasing, the as-quenched samples were aged and simultaneously gas nitrided at 470 °C for 50 min in a N_2-H_2 atmosphere containing 7% NH_3. The nitriding potential was 3.8 $atm^{-1/2}$.

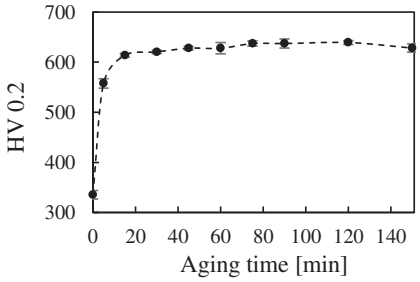

Fig. 1. Vickers hardness of the studied maraging steel as a function of aging time at an aging temperature of 470 ± 5 °C.

Glow discharge optical emission spectroscopy depth profiles were recorded with a Spectruma GDA 750 GD-OES analyzer. The samples for electron backscatter diffraction (EBSD) examination were prepared by electropolishing with A2 Struers electrolyte, followed by mechanical polishing with OP-U for 40 min. EBSD data were collected by an Oxford-HKL EBSD system attached to a FEI Nova 600 Nanolab Dual Beam FIB-SEM (Focussed Ion Beam - Scanning Electron Microscope) with field emission gun. The EBSD patterns were acquired with an acceleration voltage of 18 kV, a beam current of 2.2 nA, and a step size of 60 nm. The EBSD data were postprocessed with the OIM-TSL Data Analysis 7 commercial software.

Two different types of specimens were prepared for atom probe tomography experiments. The first type of samples was prepared to study the aged material. They were prepared from the central part of the nitrided sample with a standard two-step electropolishing technique [23]. The second type of samples was prepared in order to study the nitrided layer. In this case site-specific sample preparation with the focussed ion beam scanning electron microscope (FIB-SEM FEI Versa 3D DualBeam) using the lift-out technique [24] was applied to extract samples from the nitrided diffusion zone at the sample's surface. The last step of the annular milling was done at 5 kV followed by a cleaning step at 2 kV to minimize Ga implantation. The atom probe tomography experiments were carried out on a local electrode atom probe (LEAP 3000X HR) from Cameca at a temperature of 60 K in voltage mode with a pulse repetition rate of 200 kHz and a pulse fraction of 20%. The Imago Visualization and Analysis Software (IVAS) version 3.6.6 was used for data reconstruction and analysis. Several peak overlaps in the mass-to-charge-state ratio spectrum are present in this highly alloyed material. Peak deconvolution was considered for the overlapping peaks based on the natural abundance of the present elements: for the Ni^{2+} and Fe^{2+} overlap at 29 Da, for Mo^{3+} and Ni^{2+} at 32 Da, for N^+ and Si^{2+} at 14 and 15 Da, and the N_2^+ and Fe^{2+} overlap at 28 Da.

In order to study the aged material with TEM, the nitrided layers were removed by grinding and polishing up to 60 µm, keeping the central and aged material. Subsequently, the samples were thinned by means of a twin-jet electropolishing setup (Struers Tenupol-5) using a mixture of 4 vol% perchloric acid and 96 vol% acetic acid at room temperature. In order to study the nitrided layer, the Focused Ion Beam and lift-out method (FIB-SEM, FEI Nova 600 Nanolab DualBeam) was applied on the outer layer of the nitrided part. High-resolution transmission electron microscopy (HRTEM) and selected area electron diffraction (SAED) were performed using an objective lens C_s corrected JEOL JEM-2200FS FEG TEM operating at 200 kV. The images were analyzed with the Digital Micrograph™ software (Gatan, USA). To interpret the SAED patterns, diffraction patterns were simulated with the JEMS software [25].

Density Functional Theory (DFT) [26,27] calculations were performed at 0 K and zero pressure to study the atomic structure of the nitrides. The ACONVASP software package [28] was used to construct the starting unit cells. All DFT calculations were carried out on the

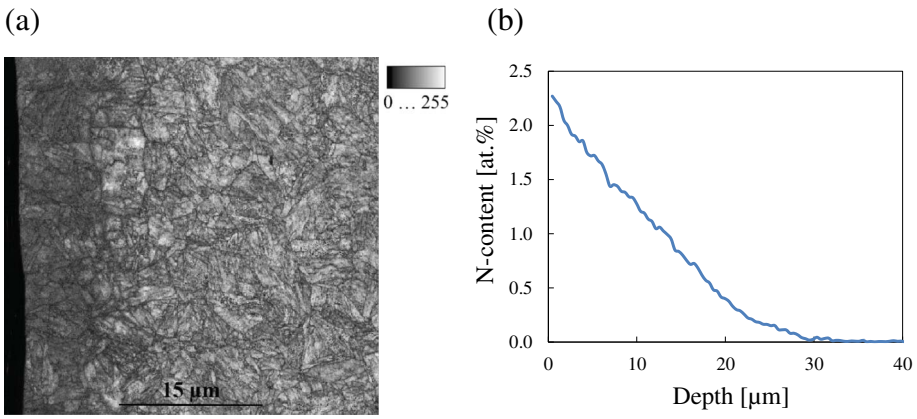

Fig. 2. (a) Band slope parameter map. Dark pixels correspond to distorted crystal lattices. (b) GD-OES N profile of the studied nitrided maraging steel.

Table 1
Chemical analysis of the maraging steel (optical emission spectroscopy) and chemical analysis measured by APT (at.%).

at.%	Fe	Co	Ni	Mo	C	Al	Si	Cr	Mn	Cu
Comp.	Bal.	16.25	18.03	3.23	0.024	0.054	0.091	0.066	0.075	0.072
APT	61.6 ± 0.25	16.5 ± 0.19	18.1 ± 0.42	3.4 ± 0.01	0.01 ± 0.002	0.06 ± 0.002	0.05 ± 0.06	0.09 ± 0.001	0.08 ± 0.001	0.05 ± 0.001

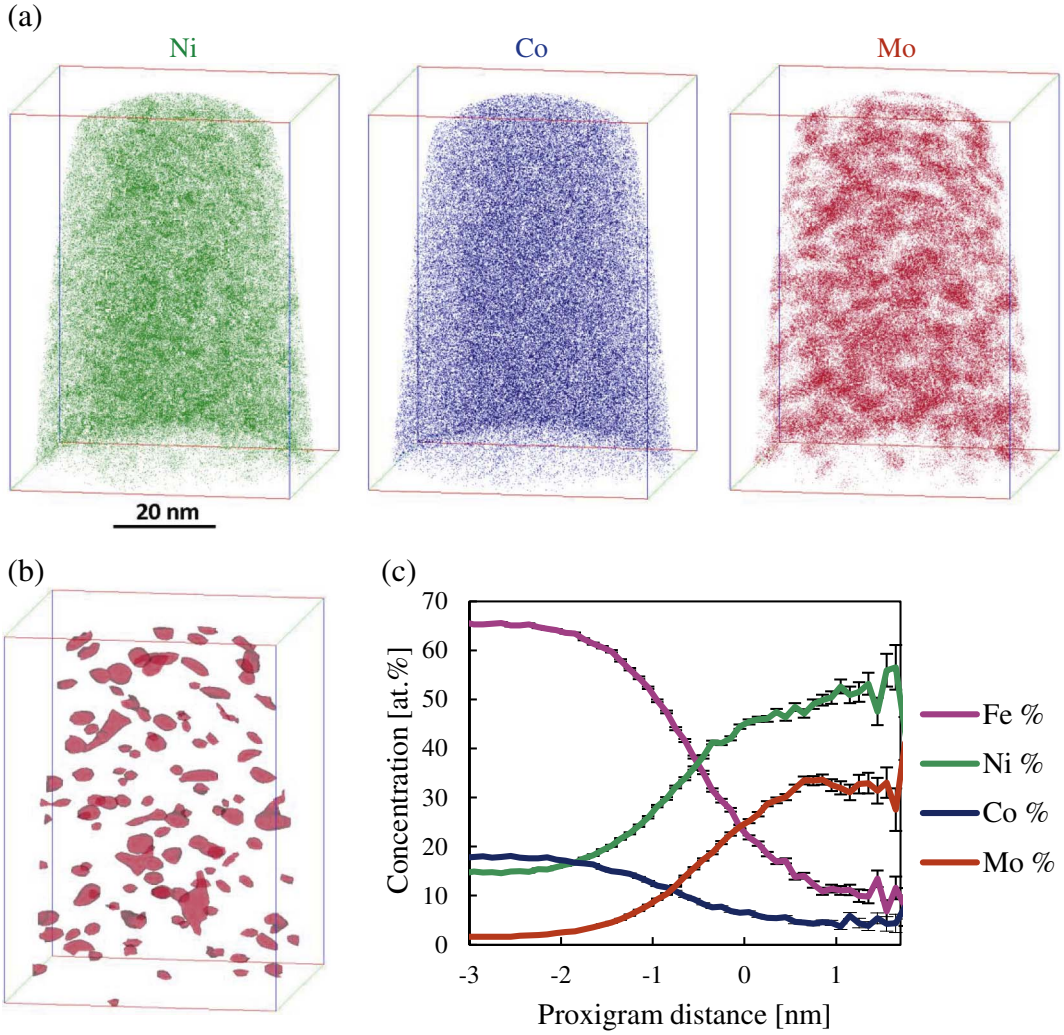

Fig. 3. Maraging steel aged at 470 °C for 50 min: (a) 3D reconstruction of the atom positions of Ni, Co and Mo; (b) Isoconcentration surfaces for 15 at.% Mo; (c) Proximity histogram according to isosurfaces with 15 at.% Mo. Zero distance on the x-axis corresponds to the precipitate/matrix interface, positive values to the precipitate.

Table 2
Chemical composition of the precipitates of aged maraging steel, based on the volumes in the isoconcentration surfaces of certain at.% Mo.

at.%	all	Inside 15 at.% Mo	Inside 18 at.% Mo	Inside 21 at.% Mo
Fe	61.6 ± 0.25	18.9 ± 1.53	15.3 ± 3.20	13.7 ± 5.66
Co	16.5 ± 0.19	5.8 ± 0.42	5.2 ± 0.81	5.0 ± 1.35
Mo	3.4 ± 0.01	29.2 ± 0.79	32.9 ± 0.98	35.9 ± 1.93
Ni	18.1 ± 0.42	45.0 ± 2.95	45.3 ± 5.40	43.8 ± 10.12
$Ni_{x=...}Mo$		1.6 ± 0.14	1.4 ± 0.21	1.2 ± 0.34
Vol%		1.1 ± 0.15	0.4 ± 0.08	0.1 ± 0.04

GGA-PBE (Perdew-Burke-Ernzerhof parametrization of the Generalized Gradient Approximation) [29] level of theory with the Vienna Ab Initio Simulation Package (VASP) software [30–34], with VASP 5.2 recommended PAW (Projector Augmented Wave) potentials [35,36]. These potentials were recently shown to provide a similar precision as all-electron calculations [37]. A $\overline{k}$-point mesh of 30 × 30 × 1 and cut-off energy of 500 eV were used for optimizing the unit cells and atomic positions, and a 40 × 40 × 1 mesh combined with a 650 eV cut-off energy for obtaining the final energies. A convergence criterion of 10^{-8} eV was used for the electronic self-consistent cycle and of 10^{-6} eV for the structural optimization. For electronic convergence, Methfessel-Paxton smearing [38] (σ = 0.2 eV) was used for structure optimization and the tetrahedron method with Blöchl corrections [39] for the final energies.

3. Results

3.1. Aging Response

Hardness measurements of the maraging steel aged for different times at a temperature of 470 ± 5 °C are presented in Fig. 1. A hardness plateau is visible after 20 min of aging and a remarkable increase in hardness can already be observed after 5 min. The very fast aging response is associated with the high Co content [8]. An aging time of 50 min was selected for this work, in order to have an adequate nitriding depth as well.

3.2. Thickness of the Nitrided Layer

The microstructure of the nitrided layer and the substrate, represented with the band slope map derived from the diffraction pattern [40,41], is shown in Fig. 2a. The band slope parameter represents the intensity gradient observed at the margins of the Kikuchi lines in the electron backscatter diffraction pattern (EBSP) [42]. Darker pixels in the map have lower band slope parameter values which correspond to a distorted matrix, in this case the nitrided diffusion layer. Fig. 2b displays the distribution of N through the sample thickness measured with GD-OES. After nitriding, no compound layer was formed at the surface. Only a diffusion zone and a transition zone from this diffusion zone to the core material, with a total thickness of around 20 μm, are visible in the GD-OES depth profile of N. The effective nitrided layer thickness according to the band slope map is around 10 μm, which corresponds to a threshold for N of around 1.2 at.%. Residual stress measurements by the micro-slit milling method were executed on the nitrogen diffusion zone of the same steel grade with different nitriding thicknesses and

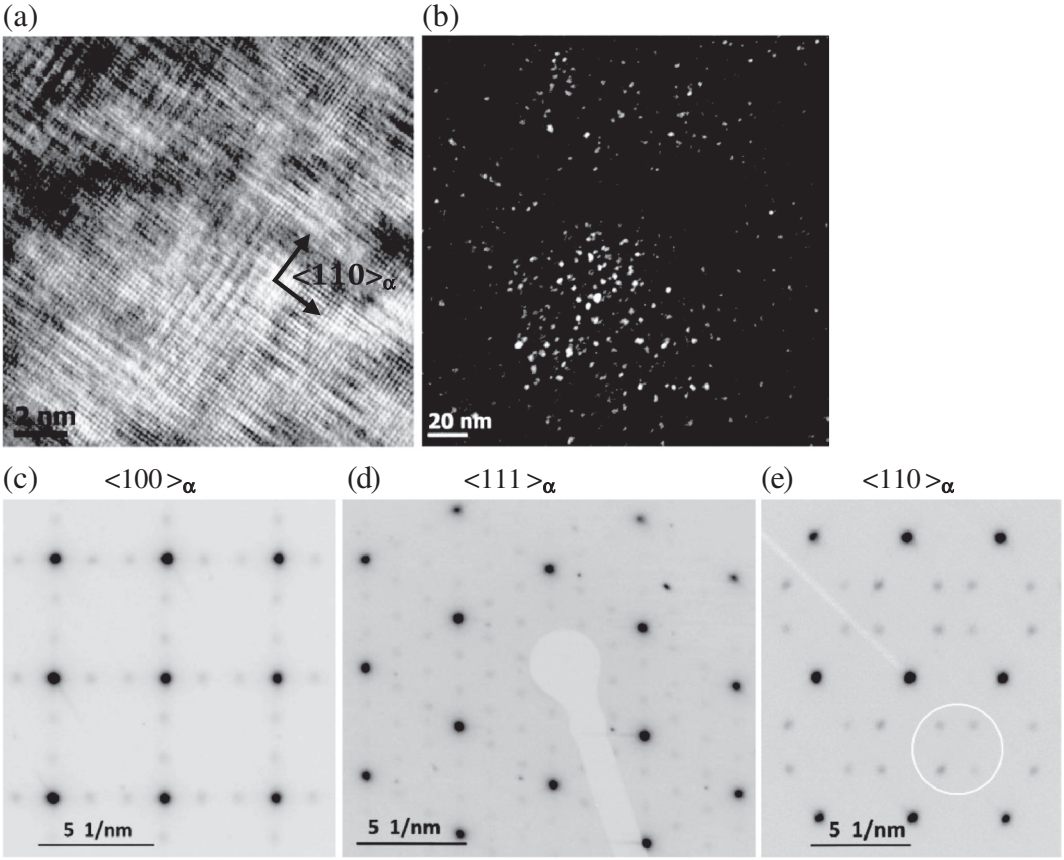

Fig. 4. Maraging steel aged at 470 °C for 50 min: (a) < 100 > $_\alpha$ HRTEM image, (b) The dark field micrograph from the circle in (e) showing the presence of precipitates, (c) SAED corresponding to < 100 > $_\alpha$ zone axis showing superlattice reflections, (d) < 111 > $_\alpha$ zone axis diffraction pattern, (e) < 110 > $_\alpha$ zone axis diffraction pattern.

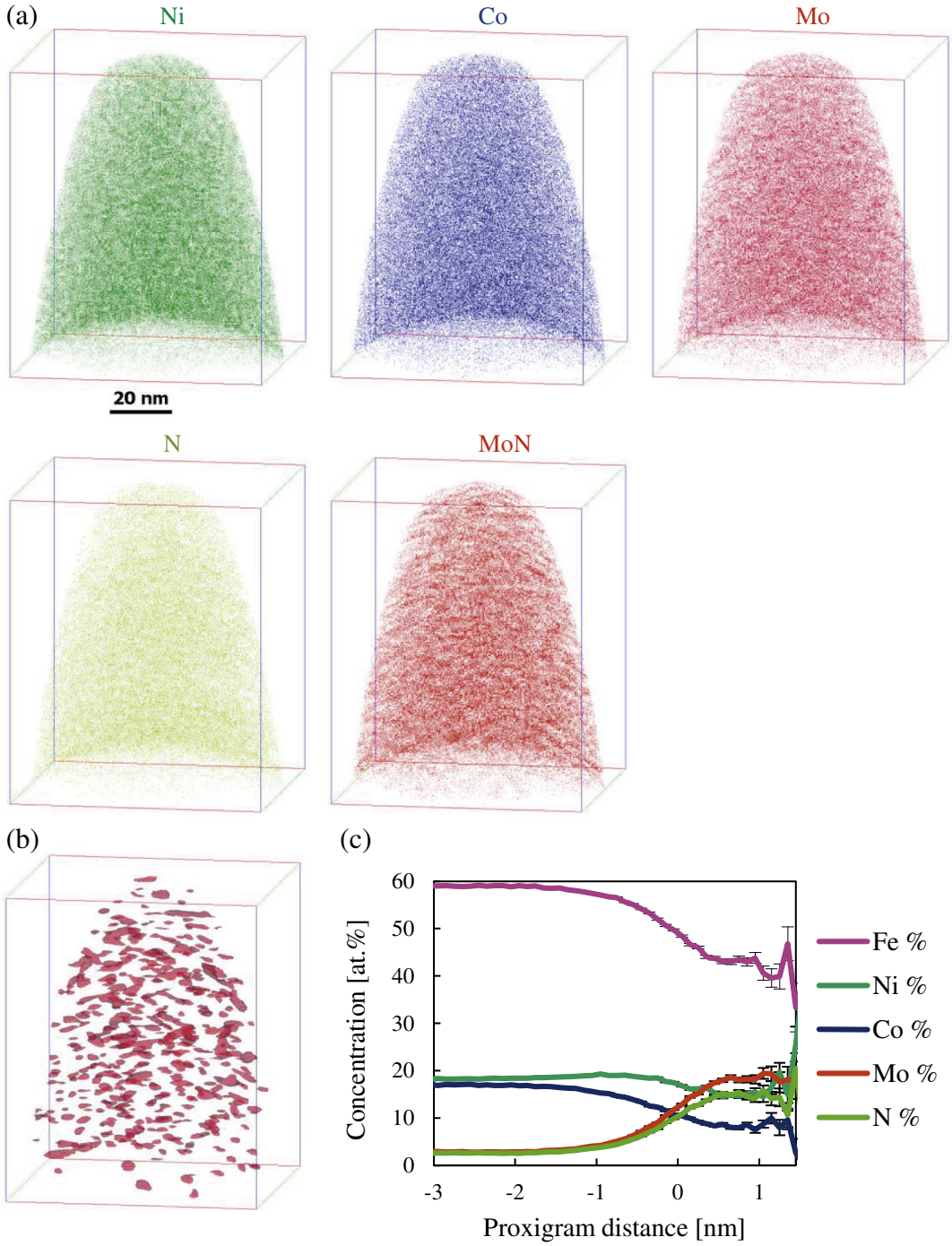

Fig. 5. Sample nitrided at 470 °C for 50 min: 3D reconstruction of the atom positions of (a) Ni, Co, Mo, N and MoN molecules; (b) Isoconcentration surfaces for 7.5 at.% Mo; (c) Proximity histogram according to isosurfaces with 7.5 at.% Mo.

Table 3
Average chemical composition of the precipitates in the maraging steel nitrided at 470 °C for 50 min, based on the volumes in the isoconcentration surfaces of certain at.% Mo.

at.%	all	Inside 7.5 at.% Mo	Inside 9 at.% Mo	Inside 10.5 at.% Mo
Fe	58.4 ± 0.25	46.8 ± 0.69	43.2 ± 0.71	40.7 ± 0.32
Co	16.4 ± 0.13	9.8 ± 0.28	8.6 ± 0.24	7.9 ± 0.91
Mo	3.4 ± 0.10	14.5 ± 0.58	17.9 ± 0.71	20.6 ± 0.50
Ni	18.6 ± 0.25	16.2 ± 0.42	15.0 ± 0.64	13.4 ± 0.55
N	3.0 ± 0.16	12.1 ± 0.69	14.7 ± 0.76	16.8 ± 0.74
$MoN_{x=...}$		0.84 ± 0.03	0.82 ± 0.02	0.80 ± 0.03
Vol%		1.23 ± 0.27	0.26 ± 0.06	0.05 ± 0.01

reported in [43]. Both the microstructure in the aged bulk material and in the first 1–2 μm of the nitrided diffusion zone are studied.

3.3. Microstructure of the Aged, Not Nitrided Maraging Steel

3.3.1. APT Study of the Aged Steel

Table 1 lists the chemical composition of the steel measured both with optical emission spectroscopy and with atom probe tomography. It can be observed that these compositions match well. The three-dimensional reconstruction of the positions of Ni, Co and Mo atoms in the aged sample based on the APT results is presented in Fig. 3a. Significant clustering of Mo atoms is observed, whereas the clustering of Ni is also

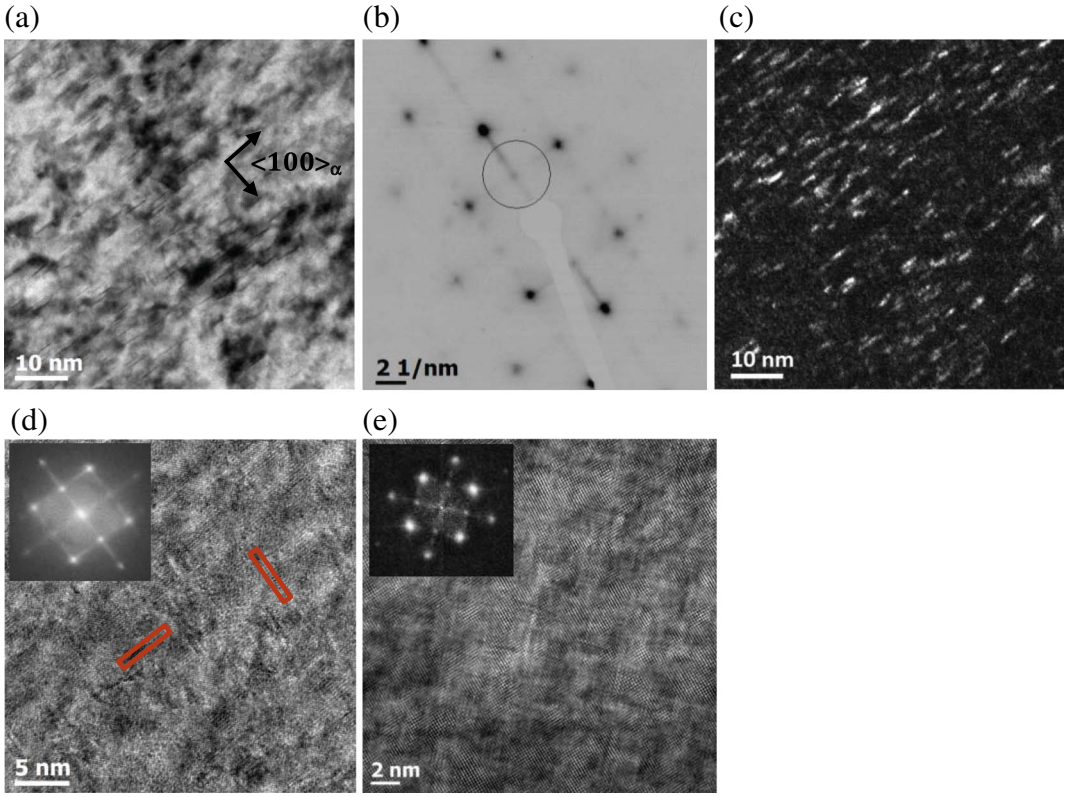

Fig. 6. Specimen nitrided at 470 °C for 50 min: (a) BF image showing nitride platelets embedded in a martensitic matrix; (b) SAED of (a), zone axis < 100 > ; (c) DF image, aperture indicated with circle in (b); (d) and (e) HRTEM and Fourier transform showing two sets of perpendicular platelets embedded in a martensitic matrix, zone axis < 100 > .

Table 4
Atomic coordinates within the P-3 trigonal phase of $(Fe,Ni)_7Mo_2$ and $(Fe,Ni)_8Mo$.

Ni_7Mo_2 *(Ni_8Mo)*	Wyckoff position	a = $a_\alpha \sqrt{6}$ x	b = $a_\alpha \sqrt{6}$ y	c = $a_\alpha \frac{\sqrt{3}}{2}$ z
Fe, Ni *(Mo)*	1a	0	0	0
Fe, Ni	6 g	1/3	0	1/3
Mo *(Fe, Ni)*	2d	1/3	2/3	0

apparent, but less pronounced. Isoconcentration surfaces of 15 at.% Mo are used for visualization of the precipitates, which appear to be randomly distributed in the matrix (Fig. 3b). The same type of nanometer-sized precipitates are observed by TEM as spherical particles (see Section 3.3.2), allowing for proper adjustment of the APT reconstruction parameters to obtain spherical precipitates [44]. The proximity histogram in Fig. 3c, which is the average concentration profile over all precipitates normal to the isoconcentration surface, shows that the precipitates have a high Mo and Ni content, while Fe and Co contents are quite low but do not drop to zero. In order to determine the chemical composition of the precipitates, the volumes in the isoconcentration surfaces of 15, 18 and 21 at.% Mo are considered in Table 2. The average volume of a precipitate is 18.7 nm^3 (or a calculated diameter of 3.3 nm if it is assumed that all precipitates are spherical) and the vol% of precipitates in the measurement is 1.1%, based on the volumes in the isoconcentration surface of 15 at.% Mo. As it can be seen from the result in Table 2, the vol% decreases quickly when higher threshold values are considered, therefore 15 at.% Mo was chosen for an estimation of the dimensions. In addition, due to evaporation aberrations a lot of Fe ions from the matrix are included in the particles and the dimensions are overestimated.

3.3.2. TEM Study of the Aged Material

TEM images were acquired from the sample aged at 470 °C for 50 min. Imaging in high resolution (Fig. 4a) reveals regions having an ordered structure with a periodicity of planes in the < 110 > direction in every third atomic layer. No clear interfaces are visible in this bright field image and the precipitates cannot be distinguished from the matrix, which could be explained by their high density and coherent boundaries. The dark field micrograph (Fig. 4b) taken using superlattice spots, indicated with the circle in Fig. 4e, shows circular precipitates having an average diameter of 2.3 ± 0.7 nm. This is slightly smaller than the diameter deviated from APT measurements. The selected area diffraction patterns in Fig. 4 c–e, reveal superlattice reflection spots, such as the maxima at 1/3 and 2/3 < 110 > directions in the < 100 > bcc pattern of the matrix (Fig. 4c).

3.4. Microstructure of the Nitrided Layer After Simultaneously Aging and Nitriding

3.4.1. APT Study of the Nitrided Zone

Fig. 5a shows the 3D reconstruction of Ni, Co, Mo and N atoms, as well as MoN molecules. Clustering of MoN and a bit less pronounced clustering of Mo can be observed. This can be explained by the rather strong cohesive energy of the MoN pairs [45]. Isoconcentration surfaces of 7.5 at.% Mo are used for visualization of the precipitates in Fig. 5b. In this calculation the MoN molecules are broken down to their constituent atoms. Peak overlap can occur for N_2^+ and Fe^{2+} at 28 Da, which could lead to an underestimation of the actual nitrogen concentration [46,47]. The mass spectra of the volumes inside the isoconcentration surfaces of 7.5, 9 and 10.5 at.% Mo were analyzed. In these nitrides, the observed ion abundances for 27, 28 and 28,5 Da fit to the natural abundances of the isotopes of Fe. Therefore only a negligibly small amount of N_2^+ ions can be hidden beneath the Fe^{2+} peak at

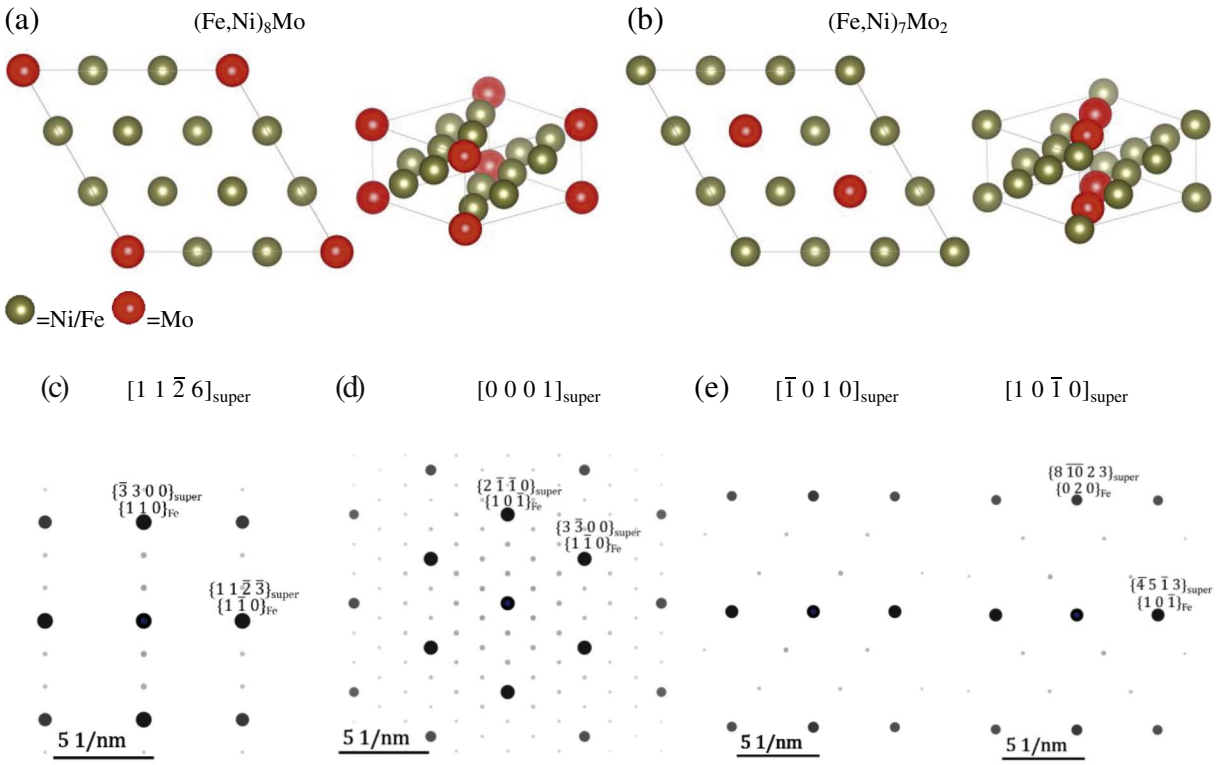

Fig. 7. Reconstructed atomic positions for (a) $(Fe,Ni)_8Mo$: view along c-axis and perspective view, (b) $(Fe,Ni)_7Mo_2$: view along c-axis and perspective view, (c) simulated diffraction spots, zone axis [1 1 $\bar{2}$ 6], (d) simulated diffraction spots, zone axis [0001], (e) simulated diffraction spots, two variants zone axis [$\bar{1}$ 0 1 0] and zone axis [1 0 $\bar{1}$ 0].

28 Da. The proximity histogram (Fig. 5c), in this case the average concentration profile normal to the isoconcentration surfaces of 7.5 at. % Mo, shows that the precipitates are richer in Mo and N and leaner in the other alloying elements and Fe. In order to determine the chemical composition of the precipitates, the volumes in the isoconcentration surfaces of 7.5, 9 and 10.5 at.% Mo are considered in Table 3. Being just an indication for a possible precipitate, the ratio of N to Mo is calculated and is around 0.8. The average volume of a precipitate is 13.12 nm^3 and the vol% of precipitates in the measurement is 1.23%, based on the volumes in the isoconcentration surface of 7.5 at.% Mo.

3.4.2. TEM Study of the Nitrided Zone

TEM images of the nitrided diffusion zone are shown in Fig. 6. The TEM bright field image (Fig. 6a) reveals interrupted lines parallel to the < 100 > directions of the bcc matrix. Both streaks and additional reflections can be found on the 001 diffraction pattern (Fig. 6b). The dark field image from one of the additional reflections also reveals fine platelets on the {100} bcc matrix planes (Fig. 6c). A large density of small precipitates is also observed in HRTEM, as shown in Fig. 6d–e, where two sets of perpendicular platelets embedded in a martensitic matrix are visible. The diameter of the platelets lying on the {100} planes of the martensitic bcc matrix is 3.7 nm ± 2.3 nm. The continuity of atomic planes across the platelets can be observed, indicating full coherency with the Fe-matrix.

4. Discussion

4.1. Atomic Structure of the Intermetallics in the Aged Maraging Steel

A high density of precipitates is observed both by APT and TEM in the maraging steel after only 50 min of aging. This can be explained by the high Co content which reduces the solubility of Mo in the bcc matrix, and therefore increases the driving force for the precipitation of Mo-rich phases [8]. It is reported that during the early stages of aging, short-range ordering results in Fe-Co regions and Ni-rich regions (Ni-Mo-Ti) [48], which facilitates the precipitation of usually coherent and Ni-rich intermetallic compounds Ni_3Mo or Ni_3Ti in a later stage of aging.

The fraction of Fe which is observed with APT in the precipitates of the aged material can differ slightly from the real fraction due to trajectory overlaps and local magnification [49] and is expected to be overestimated but not necessarily zero [50]. The superlattice reflection spots in the SAED patterns in Fig. 4 can be explained in the real lattice by an ordered arrangement of atoms of different atomic scattering powers, where the ordered structure is derived from the bcc lattice. As the atomic scattering factor depends on the atomic number, the components of the alloy can be divided into a group of Fe, Ni and Co and a group of Mo. The observed diffraction patterns were also reported in [3,7,51,52] for similar alloys, and interpreted as the ordered hexagonal ω-phase, sometimes called the S-phase, $(Fe,Ni)_8Mo$ or $(Fe,Ni)_7Mo_2$. The precipitates of the ω-phase are reported to be small, quasi-spherical and a precursor of Ni_3Mo [53]. According to [51], the diffraction spots belong to $(Fe,Ni)_7Mo_2$ with a hexagonal $P6_3/mmc$ structure. However, the current study shows that a better description of this $(Fe,Ni)_8Mo$ or $(Fe,Ni)_7Mo_2$ phase is the trigonal P-3 structure with parameters: a = 0.702 nm and c = 0.248 nm, as described in Table 4 and Fig. 7. The a-axis of the superstructure corresponds to $[11\bar{2}]_\alpha$, the b-axis to $[\bar{2}11]_\alpha$, and the c-axis to $[111]_\alpha$. Yedneral and Perkas [54] proposed a continuous evolution of A_8B, through A_7B_2 up to A_6B_3 or the known A_2B ω-phase, with A = Fe, Ni, Co, and B = Mo. The rhombohedral A_2B ω-phase shows less superlattice spots in the diffraction pattern and does not fit to the experimental diffraction pattern in this work. Both $(Fe,Ni)_8Mo$ and $(Fe,Ni)_7Mo_2$ lead to the same diffraction patterns. Multiple variants of the omega phase were formed, as can be seen in Fig. 7 c and e. Being only an indication for the composition of the precipitates measured with APT, the ratio of Ni to Mo is around 1.6 and the ratio of Fe and Ni to Mo is around 2.2. This is lower than what is expected from the TEM analysis and can be explained by the continuous evolution from A_8B, through A_7B_2 up to A_2B [54], where it seems that the composition of the precipitates is close to A_2B. For higher threshold values

Table 5
Overview of Mo-N-Fe structures and corresponding cohesive energies from DFT calculations, based on the equations in the 2nd column. Structure 1 and 2 are Mo-N monolayers, structure 3–5 correspond to double layers of Mo and N, where structure 5 has a 1–1 stoichiometry. Structure 6–7 correspond to Mo-N triple layers, with structure 7 having the 1–1 stoichiometry. Structure 8 is an ordered structure of Mo-N layers on every fourth layer of Fe.

1.	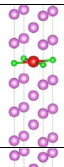	$Fe_{19}Mo(s) + \frac{1}{2}N_2(g) \leftrightarrows Fe_{19}MoN(s)$	$\Delta U = -47\frac{kJ}{mol\ N}$
2.	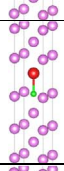	=Fe =Mo =N	$\Delta U = -31\frac{kJ}{mol\ N}$
3.	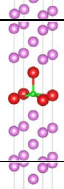	$Fe_{18}Mo_2(s) + \frac{1}{2}N_2(g) \leftrightarrows Fe_{18}Mo_2N(s)$	$\Delta U = -93\frac{kJ}{mol\ N}$
4.	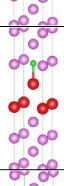		$\Delta U = -25\frac{kJ}{mol\ N}$
5.	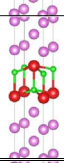	$Fe_{18}Mo_2(s) + N_2(g) \leftrightarrows Fe_{18}Mo_2N_2(s)$	$\Delta U = -76\frac{kJ}{mol\ N}$
6.	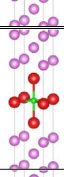	$Fe_{17}Mo_3(s) + \frac{1}{2}N_2(g) \leftrightarrows Fe_{17}Mo_3N(s)$	$\Delta U = -149\frac{kJ}{mol\ N}$
7.	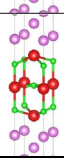	$Fe_{17}Mo_3(s) + \frac{3}{2}N_2(g) \leftrightarrows Fe_{17}Mo_3N_3(s)$	$\Delta U = -60\frac{kJ}{mol\ N}$
8.	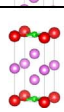	$Fe_{19}MoN(s) \leftrightarrows Fe_3MoN(s) + 16Fe(s)$	$\Delta U = -22\frac{kJ}{mol\ N}$

of Mo, the uncertainty of the Ni content increases (Table 3), which could be linked to small deviations in the chemical composition of the precipitates in the transition state. These observations confirm the existence of the known ω-phase.

4.2. Atomic Structure of the Nitrides

The small precipitates or clusters which are detected in the nitrided diffusion zone are still in the early stage of precipitation. No intermetallics could be observed in the first few micrometers of the nitrided layer. APT shows that the Fe content decreases in the nitrides but is remarkably higher than in the intermetallic precipitates, probably due to the trajectory overlap between the matrix and the very thin plate-like precipitates. In this case, the influence from the matrix on the chemical composition of the precipitates is considerable. It was observed that the ion density is lower inside the particles, which is associated with the higher evaporation field of the precipitates. For high field precipitates, trajectory overlaps of around 1 nm are expected outside the precipitate nearby the interface [55]. Besides, lateral surface diffusion of mainly interstitial atoms on the APT tip can affect the N content of matrix and precipitates. For very fine platelets, the local magnification effect can lead to erroneous detection of large amounts of Fe in the platelets [47]. However, in the very early stage of precipitation the precipitates genuinely still contain a lot of Fe. The observed precipitates could be Mo-nitrides or $Fe_xMo_yN_z$ zones.

Streaks in the diffraction pattern in the < 001 > direction (Fig. 6b) are ascribed to both small dimensions of the scattering object of precipitates or GP zones and irregular spatial distribution between them along the direction parallel to the streaks [56]. The additional reflections in the diffraction pattern can appear due to B2 ordering. The observed precipitates could also be assigned to the FCC-Mo_2N phase, obeying the Baker-Nutting orientation relationship with the matrix: $\{100\}_{nitride}//\{100\}_{\alpha}$ and $< 001 >_{nitride}// < 011 >_{\alpha}$ [20,57]. However, the simulated diffraction pattern does not fit exactly with the observed SAED pattern. Selg et al. [58] concluded that largely coherent Mo_2N-type nitrides develop in maraging steel upon nitriding, surrounded by a tetragonally distorted matrix. Mobile and immobile excess nitrogen is expected in solution-annealed maraging steel which is nitrided. The immobile excess nitrogen is adsorbed at the precipitate/matrix interface, while the mobile excess nitrogen is dissolved in the strained matrix. This excess nitrogen could explain deviation from a specific stoichiometry in the early stages of precipitation. Individual atomic columns composing the platelets in Fig. 6d–e indicate that the platelets consist of a monolayer. However, according to these HRTEM images the platelets could be up to three atomic layers thick but due to the limited resolution they cannot be sharply visualized. The observed structure is expected to be similar to a Mo_2N monolayer which is coherent with the surrounding, tetragonally distorted Fe-matrix. This possible structure was investigated further and is discussed below.

Since TEM and APT do not lead to an unambiguous conclusion regarding the nitrides, DFT calculations have been carried out. The main objective is to obtain optimized structures which correspond to the observed diffraction patterns. Additionally, the relative stabilities of different coordinations of the N atoms can be determined. To isolate a single precipitate in a three-dimensional periodic code, unit cells of 20 layers of Fe in the < 100 > direction were constructed using the ACONVASP software and a number of Fe atoms were replaced with one, two or three consecutive layers of Mo atoms. This number of layers separates the periodic repetition of the Mo precipitates by > 2.5 nm, which is sufficient to cut out all electronic interactions. In a first step, the atomic positions of those structures and the unit cell shape and volume were allowed to relax using a conjugate-gradient algorithm. This results in a fully optimized structure under zero pressure. Secondly, N atoms were introduced into the different octahedral interstitial sites available in the Mo layers, again fully optimizing the unit cell. This enables to determine the energetically most favorable site for N. Finally, Mo-N precipitates of varying thickness with a 1-1 stoichiometry, where the N atoms are placed in the most favorable octahedral positions, were optimized and their cohesive energies were calculated.

When the N atoms are in the octahedral sites in the Mo plane, with two Mo atoms of that plane as nearest neighbors, the difference in cohesive energy ΔU corresponds to 197 $\frac{kJ}{mol\ N}$ in a monolayer, and to 130 $\frac{kJ}{mol\ N}$ in a triple Mo layer. This configuration is highly unfavored, as can be expected on simple geometric grounds. The precipitate plane is coherent with the bulk Fe matrix, which entails that the Mo atoms in that plane are only the lattice parameter of bulk Fe apart. An energetically costly orthorhombic distortion takes place if the N atom is inserted between those Mo atoms. If the two octahedral neighbors of the N atom are coordinated perpendicular to the precipitate, the tetragonal distortion already caused by the Mo precipitate atoms forms an

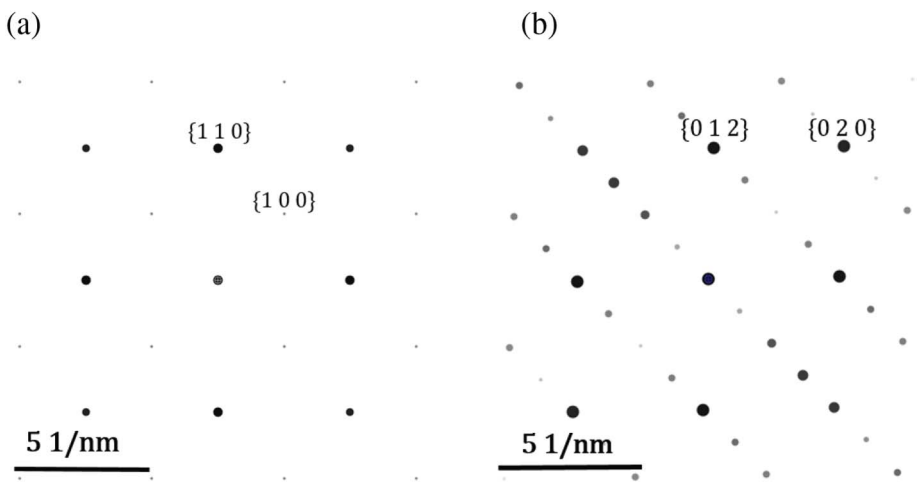

Fig. 8. (a) Simulated diffraction pattern of structure 1 of Table 5, zone axis [001], (b) Simulated diffraction pattern of structure 8 of Table 5, zone axis [100]. Both patterns correspond well to Fig. 6b.

ideal position for the N atom. Table 5 shows the preferential octahedral sites of the interstitial N atoms and their corresponding cohesive energies. For the energetic comparisons, bulk bcc Fe and bcc Fe with N in the octahedral position were also optimized and the enthalpy of solution is calculated to be $\Delta U = 14\ \frac{kJ}{mol\ N}$. It is clear that N has a higher affinity for Mo than for Fe. In the case of a monolayer of Mo, the N prefers to be in the Mo-layer, with Fe as nearest neighbors (cf. Table 5, structure 1). However, a N atom positioned just outside the Mo layer (cf. Table 5, structure 2) is energetically quite similar. The same conclusion can be drawn for the double Mo layer (cf. Table 5, structure 3 and 4 respectively). Structure 6, the triple Mo layer, has the lowest cohesive energy. To assess the driving force for growth of the Mo-N precipitates in the z-direction, the cohesive energy of the single-layer structure (cf. Table 5, structure 1) is compared to the cohesive energy of the double- and triple-layer structure (cf. Table 5, structure 5 and 7 respectively). The combination of two single layers into a double Mo-N layer corresponds to a cohesive energy difference of $\Delta U = -26\ \frac{kJ}{mol\ N}$ $(2\ Fe_{19}MoN \leftrightarrows Fe_{18}Mo_2N_2 + 20\ Fe)$. For the combination of three single layers into a triple layer, ΔU $(3\ Fe_{19}MoN \leftrightarrows Fe_{17}Mo_3N_3 + 40\ Fe)$ equals $-2\ \frac{kJ}{mol\ N}$. It can be concluded that the driving force to create multiple layers exists but is relatively small, which results in the predominance of single-layer Mo-N precipitates for short nitriding treatments, as evidenced by the TEM results (see Fig. 6d and Fig. 6e).

Fig. 8a shows that the simulated diffraction pattern of the Mo-N monolayer in Fe (structure 1 in Table 5) corresponds well to the SAED patterns in Fig. 6b. Also structures 2 to 7 lead to the simulated diffractions pattern of Fig. 8a. The position of N has a limited impact on the SAED, but the position of the Mo in the Fe-lattice can be linked to B2 ordering and the corresponding additional reflections in the diffraction pattern. However, extra satellites appear in the experimental diffraction pattern which could be explained by an ordered structure of the Mo-N layers which form on every fourth layer of Fe (cf. Table 5, structure 8 and Fig. 8b). There is also an affinity of the Mo layers to form this structure, but the driving force is not very large. A similar structure of single-layered NbN GP zones in steel was reported in [59] with an uncertainty of the position of the N atoms. The compression of the lattice parameter of Fe in the direction perpendicular to the precipitate with the precipitate as nearest neighbor is 2.1% for the Mo-N monolayer. The desired expansion of the nitrided layer as compared to the unnitrided core leads to the compressive macrostress parallel to the surface in the nitrided zone. The distorted Fe-matrix around the Mo-N monolayers corresponds with the microstresses and gives rise to diffraction line broadening (streaks in the SAED). This is also observed as the lower value of the band slope parameter of the EBSD data from the nitrided layer in comparison to the substrate (Fig. 2a).

5. Summary and Conclusions

Two high-resolution techniques, TEM and APT were used to study the precipitates in aged and nitrided Fe-Ni-Co-Mo maraging steel. Ni-Mo type intermetallics were found in the aged bulk material, while Mo-N precipitates were detected in the nitrided zone nearby the surface. These two different types of precipitates are uniformly distributed in the matrix and both have a volume fraction of around 1% in the zone of characterization.

The strengthening intermetallic precipitates formed during the early stages of aging were identified with the aid of TEM as the known ω-type precipitate, with chemical composition of $(Fe,Ni)_8Mo$ or $(Fe,Ni)_7Mo_2$ and a trigonal crystal lattice. However, the APT analysis shows that the (Fe,Ni) to Mo ratio is lower than the one expected in the phase identified by TEM. This can be explained by the continuous evolution of $(Fe,Ni)_8Mo$ through $(Fe,Ni)_7Mo_2$ up to the rhombohedral ω-phase $(Fe,Ni)_2Mo$, where the observed intermetallics are in the transition from $(Fe,Ni)_7Mo_2$ to $(Fe,Ni)_2Mo$, while the crystal structure still corresponds to $(Fe,Ni)_7Mo_2$. The diameter of the spherical precipitates is around 3 nm.

The first few micrometers of the nitrided layer of the simultaneously aged and nitrided maraging steel contain disc shaped precipitates on the {001} martensitic lattice. The diameter of the discs is 3–4 nm, while their thickness is estimated to be one atomic layer. APT reveals the enrichment of the precipitates in Mo and N. However, some influence of the matrix on the chemical composition is present since the precipitates are very small. DFT calculations were performed to compare different configurations of the N atom in Mo-N precipitates of varying thickness. The energetically most favorable position of the N atom is the octahedral position inside the Mo layers, with the nearest neighbor pair oriented perpendicular to the precipitate plane. The low driving force to stack the Mo-N layers agrees with the predominance of single-layer precipitates observed in TEM.

Acknowledgements

The authors acknowledge the financial support of the Dutch Materials Innovation Institute (M2i) under the contract M21.10.11442.

References

[1] W. Sha, A. Cerezo, G.D.W. Smith, Phase chemistry and precipitation reactions in maraging steels: part I. Introduction and study of Co-containing C-300 steel, Metall. Trans. A. 24A (1993) 1221–1232.
[2] S.J. Kim, C.M. Wayman, Precipitation behavior and microstructural changes in

maraging Fe-Ni-Mn-Ti alloys, Mater. Sci. Eng. A128 (1990) 217–230.
[3] J.M. Genin, G. Le Caer, Mössbauer study of precipitation in Fe-Ni-Mo and Fe-Ni-Co-Mo maraging alloys, Scr. Metall. 8 (1974) 15–22.
[4] B. Pennings, M. Tran, M. Derks, A. Brandsma, B. Boulogne, J. Davidson, New push-belt design to increase power density of CVTs featuring a new maraging steel, Proceedings of the Fisita World Automotive Congress, 2004.
[5] W. Sha, G.D.W. Smith, A. Cerezo, Atom probe field-ion microscopy of ageing behaviour of a model Fe-Ni-Co-Mo maraging steel, Surf. Sci. 266 (1992) 378–384.
[6] R. Tewari, S. Mazumder, I.S. Batra, G.K. Dey, S. Banerjee, Precipitation in 18wt% Ni maraging steel of grade 350, Acta Mater. 48 (2000) 1187–1200.
[7] C. Servant, N. Bouzid, O. Lyon, Small-angle X-ray scattering investigation of the martensite unmixing in maraging alloy using synchrotron radiation, Philos. Mag. A 56 (1987) 565–592.
[8] W. Sha, A. Cerezo, G.D.W. Smith, Phase chemistry and precipitation reactions in maraging steels: part III. Model alloys, Metall. Trans. A. 24A (1993) 1241–1249.
[9] J. Fernández de Ara, E. Almandoz, J.F. Palacia, G.G. Fuentes, R.J. Rodriguez, J.A. Garcia, Influence of temperature in arc-activated plasma nitriding of maraging steel in solution annealed and aged conditions, Surf. Coat. Technol. 258 (2014) 754–762.
[10] S.R. Meka, E.J. Mittemeijer, Abnormal nitride morphologies upon nitriding iron-based substrates, JOM 65 (2013) 769–775.
[11] S. Lampman, Heat Treating: Surface Hardening of Steels, 4 ASM, 1991.
[12] M.H. Biglari, C.M. Brakman, E.J. Mittemeijer, S. Van der Zwaag, The kinetics of the internal nitriding of Fe-2at.%Al alloy, Metall. Mater. Trans. A 26 (1995) 765–776.
[13] N.V. Diaz, Nitriding of Iron-based Alloys; Residual Stresses and Internal Strain Fields, PhD thesis (2007).
[14] S.S. Hosmani, R.E. Schacherl, E.J. Mittemeijer, Nitriding behavior of Fe-4wt%V and Fe-2wt%V alloys, Acta Mater. 53 (2005) 2069–2079.
[15] R. Wagner, S.S. Brenner, Morphology and chemistry of internally nitrided Fe-3at.% Mo, Acta Metall. 26 (1978) 197–206.
[16] D. Isheim, E.J. Siem, D.N. Seidman, Nanometer-scale solute segregation at hetero-phase interfaces and microstructural evolution of molybdenum nitride precipitates, Ultramicroscopy 89 (2001) 195–202.
[17] J.H. Driver, J.M. Papazian, The electron and field ion metallography of zones in nitrided Fe-Mo alloys, Acta Metall. 21 (1973) 1139–1149.
[18] D.L. Speirs, W. Robert, R. Grieveson, K.H. Jack, International Symposium on Metallurgical Chemistry, I.S.I, Sheffield, 1971.
[19] D.H. Jack, The structure of nitrided iron-titanium alloys, Acta Metall. 24 (1976) 137–146.
[20] H. Selg, E. Bischoff, S.R. Meka, R.E. Schacherl, T. Waldenmaier, E.J. Mittemeijer, Molybdenum-nitride precipitation in recrystallized and cold-rolled Fe-1at.pct Mo alloy, Metall. Mater. Trans. A 44 (2013) 4059–4070.
[21] G.P. Huffman, H.H. Podgurski, Mössbauer study of nitrided Fe-Mo and Fe-Ti alloys, Acta Metall. 23 (1975) 1367–1379.
[22] J. Takahashi, K. Kawasaki, K. Kawakami, M. Sugiyama, Three-dimensional atom probe analysis of chromium- and copper-added nitriding steel, Surf. Interface Anal. 39 (2007) 232–236.
[23] M.K. Miller, Atom Probe Tomography: Analysis at the Atomic Scal, (2000).
[24] M. Miller, K. Russel, G. Thompson, Strategies for fabricating atom probe specimens with a dual beam FIB, Ultramicroscopy 102 (2005) 287–298.
[25] P. Stadelmann, JEMS Java Electron Microscopy Software, (2004).
[26] P. Hohenberg, W. Kohn, Inhomogeneous electron gas, Phys. Rev. 136 (1964) 864–871.
[27] W. Kohn, L.J. Sham, Self-consistent equations including exchange and correlation effects, Phys. Rev. 140 (1965) 1133–1138.
[28] S. Curtarolo, W. Setyawan, G.L.W. Hart, M. Jahnatek, R.V. Chepulskii, R.H. Taylor, S. Wang, J. Xue, K. Yang, O. Levy, M.J. Mehl, H.T. Stokes, D.O. Demchenko, D. Morgan, AFLOW: an automatic framework for high-throughput materials discovery, Comput. Mater. Sci. 58 (2012) 218–226.
[29] J.P. Perdew, K. Burke, M. Ernzerhof, Generalized gradient approximation made simple, Phys. Rev. Lett. 77 (1996) 3865–3868.
[30] G. Kresse, J. Hafner, Ab initio molecular dynamics for liquid metals, Phys. Rev. B 47 (1993) 558–561.
[31] G. Kresse, J. Hafner, Ab initio molecular-dynamics simulation of the liquid-metal–amorphous-semiconductor transition in germanium, Phys. Rev. B 49 (1994) 14251–14269.
[32] G. Kresse, J. Furthmüller, Efficiency of ab-initio total energy calculations for metals and semiconductors using a plane-wave basis set, Comput. Mater. Sci. 6 (1996) 15–50.
[33] G. Kresse, J. Furthmüller, Efficient iterative schemes for ab initio total-energy calculations using a plane-wave basis set, Phys. Rev. B 54 (1996) 11169–11186.
[34] G. Kresse, M. Marsman, J. Furthmüller, VASP the GUIDE, (2015).
[35] P.E. Blöchl, Projector augmented-wave method, Phys. Rev. B 50 (1994) 17953–17979.
[36] G. Kresse, D. Joubert, From ultrasoft pseudopotentials to the projector augmented-wave method, Phys. Rev. B 59 (1999) 1758–1775.
[37] K. Lejaeghere, G. Bihlmayer, T. Björkman, P. Blaha, S. Blügel, V. Blum, et al., Reproducibility in density functional theory calculations of solids, Science 351 (2016).
[38] M. Methfessel, A.T. Paxton, High-precision sampling for Brillouin-zone integration in metals, Phys. Rev. B 40 (1989) 3616–3621.
[39] P.E. Blöchl, O. Jepsen, O.K. Andersen, Improved tetrahedron method for Brillouin-zone integrations, Phys. Rev. B 49 (1994) 16223–16233.
[40] A. Verdiere, V. Bliznuk, L.A.I. Kestens, R.H. Petrov, Microstructural features controlling very high cycle fatigue of nitrided maraging steel, 6th International Conference VHCF-6, Chengdu, China, 2014.
[41] L. Ryde, Application of EBSD to analysis of microstructure in commercial steels, Mater. Sci. Technol. 22 (2006) 1297–1306.
[42] S.I. Wright, M.M. Nowell, D.P. Field, A review of strain analysis using electron backscatter diffraction, Microsc. Microanal. 17 (2011) 316–329.
[43] C. Mansilla, V. Ocelík, J.T.M.D. Hosson, Local residual stress measurements on nitride layers, Mater. Sci. Eng. A 636 (2015) 476–483.
[44] O. Dmitrieva, P. Choi, S.S.A. Gerstl, D. Ponge, D. Raabe, Pulsed-laser atom probe studies of a precipitation hardened maraging TRIP steel, Ultramicroscopy 111 (2011) 623–627.
[45] A. Deschamps, F. Danoix, F. De Geuser, T. Epicier, H. Leitner, M. Perez, Low temperature precipitation kinetics of niobium nitride platelets in Fe, Mater. Lett. 65 (2011) 2265–2268.
[46] W. Sha, L. Chang, G.D.W. Smith, L. Cheng, E.J. Mittemeijer, Some aspects of atom-probe analysis of Fe-C and Fe-N systems, Surf. Sci. 266 (1992) 416–423.
[47] T. Steiner, S.R. Meka, B. Rheingans, E. Bischoff, T. Waldenmaier, G. Yeli, T.L. Martin, P.A.J. Bagot, M.P. Moody, E.J. Mittemeijer, Continuous and discontinuous precipitation in Fe-1 at.%Cr-1 at.%Mo alloy upon nitriding; crystal structure and composition of ternary nitrides, Philos. Mag. 96 (2016) 1509–1537.
[48] X. Li, Z. Yin, A computer-simulated electron diffraction analysis of precipitates in 18Ni (350) maraging steel, Mater. Lett. 23 (1995) 269–272.
[49] M.K. Miller, M.G. Hetherington, Local magnification effects in the atom probe, Surf. Sci. 246 (1991) 442–449.
[50] A. Morley, G. Sha, S. Hirosawa, A. Cerezo, G.D.W. Smith, Determining the composition of small features in atom probe: bcc Cu-rich precipitates in an Fe-rich matrix, Ultramicroscopy 109 (2009) 535–540.
[51] C. Djega-Mariadassou, L. Bessias, C. Servant, Nanocrystalline precipitates formed by aging of bcc disordered Fe-Ni-Mo alloys, Phys. Rev. B 51 (1995) 8830–8840.
[52] J.B. Lecompte, C. Servant, G. Cizeron, A comparison of the structural evolution occurring during anisothermal or isothermal treatments in the case of nickel and manganese type maraging alloys, J. Mater. Sci. 20 (1985) 3339–3352.
[53] N. Bouzid, C. Servant, O. Lyon, Anomolous small-angle X-ray scattering from a maraging alloy during martensite unmixing, Philos. Mag. B 57 (1988).
[54] A.F. Yedneral, M.D. Perkas, Crystal structure imperfections and martensitic transformations, Fis. Metal. Metalloved 33 (1972) 315.
[55] F. Vurpillot, A. Bostel, D. Blavette, Trajectory overlaps and local magnification in three-dimensional atom probe, Appl. Phys. Lett. 76 (2000) 3127–3129.
[56] D.B. Williams, C. Barry Carter, Transmission Electron Microscopy II, Diffraction, (1996).
[57] G. Miyamoto, A. Yonemoto, Y. Tanaka, T. Furuhara, T. Maki, Microstructure in a plasma-nitrided Fe–18 mass% Cr alloy, Acta Mater. 54 (2006) 4771–4779.
[58] H. Selg, S.R. Meka, M. Kachel, R.E. Schacherl, T. Waldenmaier, E.J. Mittemeijer, Nitriding behaviour of maraging steel: experiments and modelling, J. Mater. Sci. 48 (2013) 4321–4335.
[59] F. Danoix, T. Epicier, F. Vurpillot, D. Blavette, Atomic-scale imaging and analysis of single layer GP zones in a model steel, J. Mater. Sci. 47 (2012) 1567–1571.